String-like core-shell ZnCo$_2$O$_4$@NiWO$_4$ nanowire/nanosheet arrays on Ni foam for binder-free supercapacitor electrodes

Lili Ma[1] · Zhuoqing Chang[1] · Lifang Guo[1] · Tingyu Li[1] · Gang Li[1] · Kaiying Wang[1,2]

Abstract

We report the synthesis of 3D, string-like, core-shell, heterostructured ZnCo$_2$O$_4$@NiWO$_4$ nanowire/nanosheet arrays on nickel foam using a simple two-step hydrothermal method followed by an annealing process, without the needs of conventional electrode preparation. The direct growth of ZnCo$_2$O$_4$ nanowires serves both as core and mains active materials for charge storage with high mechanical stability, while the higher conductive NiWO$_4$ nanosheets act as the shell, which could provide enough voids for electrolyte accommodation and facilitate charge transfer and storage. When working as a binder-free electrode, the as-synthesized ZnCo$_2$O$_4$@NiWO$_4$ nanowire/nanosheet arrays electrode delivers a specific capacitance as high as 1782 F g^{-1} (2.14 F cm^{-2}) at a current density of 1 mA cm^{-2} and retains 95.4% of original capacitance after 5000 cycles at 5 A cm^{-2}, compared with single ZnCo$_2$O$_4$ nanowires electrode with 1300 F g^{-1} (1.04 F cm^{-2}) and 90.9%. The excellent capacitance performance demonstrates that constructing 3D, heterostructured, core-shell, nanowire/nanosheet arrays with two different binary transition metal oxides holds great potential for high-performance supercapacitors due to the synergic effects and large specific surface area.

Keywords Hydrothermal synthesis · ZnCo$_2$O$_4$@NiWO$_4$ · Core-shell structure · Supercapacitor

Introduction

Supercapacitors, as one of the most promising energy storage devices, have attracted more and more significant research attention in the past few years attributed to extremely higher energy density compared with traditional electrostatic capacitors as well as higher power density, more robust cycling life, and much more excellent reversible charge/discharge characteristics than the commonly used lithium-ion batteries [1–3]. However, their low energy densities are still the main issue, preventing them from many practical applications. To date, the investigation of supercapacitor electrodes is mainly concentrated on carbon materials and transition metal oxides and hydroxides. Generally, transition metal oxides/hydroxides, which could exhibit exceptionally high specific capacitance and energy density that surpass carbon-based active materials because they can provide efficient faradaic redox reactions, are considered promising candidate of supercapacitive electrodes and thus have been extensively investigated [4]. Recently, many binary transition metal oxides, e.g., NiCo$_2$O$_4$ [5], ZnCo$_2$O$_4$ [6], NiMoO$_4$ [7], CoMoO$_4$ [8], MnMoO$_4$ [9] and Zn$_2$GeO$_4$ [10], and MnCo$_2$O$_4$ [11], show higher electrochemical performance than single-transition metal oxides because they could provide more variable oxidation states and enhance electrical conductivities. Among them, ZnCo$_2$O$_4$, obtained by replacing one Co atom of the cobalt oxide with Zn atom, could produce high specific capacitance comparable with other binary transition metal oxides. Multifarious ZnCo$_2$O$_4$-based materials with novel nanostructure arrays (i.e., nanowires [12], nanosheets [13], nanorods [14], and nanoparticles [15]) have been successfully synthesized by different methods, such as solvothermal method [16] and simple polyol refluxing

✉ Lifang Guo
guolifang01@tyut.edu.cn

✉ Gang Li
ligang02@tyut.edu.cn

1 College of Information and Computer & Institute of Energy Innovation, Taiyuan University of Technology, Taiyuan 030024, China

2 Department of Microsystems-IMS, University of South-Eastern Norway, 3184 Horten, Norway

process [6]. For instance, cabbage-like $ZnCo_2O_4$ achieves areal capacitance 789.11 mF cm^{-2} as positive electrode [17] and hexagonal-like $ZnCo_2O_4$ reaches specific capacitance 845.7 F g^{-1} [18]. The obtained capacitance is still below theoretical level due to inefficient usage of active material since it still suffers from limited surface area and poor electrical conductivity [19]. Therefore, $ZnCo_2O_4$ combined with high conductive carbon-based materials, such as reduced graphene (rGO) [20, 21] and carbon nanotubes [22], has been developed to further improve the electrochemical performance. For instance, the specific capacitance of the nanocomposite that $ZnCo_2O_4$ combined with rGO could reach as high as 704.2 F g^{-1} [20]. Despite the great achievements being made, the specific capacitance of the developed electrode is far from the expected level for practical application. Recently, metal oxides featuring core/shell nanostructure, e.g., $ZnCo_2O_4@NiO$ [23], $ZnCo_2O_4@Ni_xCo_{2x}(OH)_{6x}$ [24], $NiCO_2S_4@NiMoO_4$ [25], $NiMoO_4@CoMoO_4$ [26], and $MnMoO_4 \cdot H_2O@MnO_2$ [27], have received extensive attention, because the integration of two kinds of pseudocapacitive materials not only increase the loading mass of active materials with high surface area but also significantly enhance the supercapacitive properties due to synergic effects. Recently, binary transition metal oxide $NiWO_4$ with a wolframite-type structure, showing higher electrical conductivity than that of NiO with the incorporation of the W atoms [21, 28, 29], has been developed for the potential application of sensors [30], catalysis [31], and electrocatalysts [32]. Therefore, constructing $ZnCo_2O_4@NiWO_4$ core-shell nanostructured electrode is promising because of the large specific surface area of 3D nanostructure and synergic effects of two different binary transition metal oxides. In this paper, a hierarchical core-shell-nanostructured electrode is fabricated by integrating two different binary transition metal oxide $ZnCo_2O_4$ nanowires with $NiWO_4$ nanosheets on Ni foams, which have never been constructed for high-performance supercapacitors. The $ZnCo_2O_4@NiWO_4$ core-shell nanowire/nanosheet arrays grown on Ni foam are fabricated via mild hydrothermal and calcination methods with predictable excellent performance. $ZnCo_2O_4$ nanowires could be directly grown on the surface of Ni foam, and then, well-dispersed $NiWO_4$ nanosheets are vertically anchored on the surface of $ZnCo_2O_4$ nanowires, avoiding the aggregation of $NiWO_4$ particles. Generally, Ni foam with 3D structure could provide large surface area and load more active material per unit area. The direct growth of $ZnCo_2O_4$ nanowires serves both as core and main active materials for charge storage, and the strong adhesion between $ZnCo_2O_4$ nanowires and Ni foam could provide higher mechanical stability and shorten the electron transfer paths. The $NiWO_4$ nanosheets act both as the shell and

high surface area active materials, and the well-distributed nanostructure with abundant free space and high electrical conductivity could provide enough voids for electrolyte accommodation and facilitate charge transfer and storage.

Experimental details

Material preparation

The raw materials of Zn $(NO_3) \cdot 6H_2O$, Co $(NO_3) \cdot 6H_2O$, $NiCl_2 \cdot 6H_2O$, $Na_2WO_4 \cdot 4H_2O$, urea (CO $(NH_2)_2$), NH_4F, and KOH with analytical pure reagent grade, which were purchased from Sino pharm Chemical Reagents, were used in the experiments without any further purification.

Pretreatment of Ni Foam

In the pretreatment procedure, Ni foams with a thickness of 1 mm were sheared to a size of 3×1 cm^2, carefully treated with acetone under ultrasonic cleaning for 15 min to wipe away the oil contamination on the surface, and then were immersed in 1 M HCl for ultrasonic cleaning to dislodge the surface oxide layers. Ni foams were rinsed in anhydrous ethanol and deionized water for 15 min by ultrasonication, respectively. The wet Ni foams were taken out and then dried for 12 h at 60 °C in a vacuum.

Preparation of Ni@ZnCo$_2$O$_4$ nanowire arrays

To synthesis $ZnCo_2O_4$ nanowires on Ni foam as a core in the core/shell nanostructured electrode, Zn $(NO_3) \cdot 6H_2O$ (0.297 g), Co $(NO_3) \cdot 6H_2O$ (0.582 g), NH_4F (0.074 g), and CO $(NH_2)_2$ (0.3 g) were dissolved in 35 mL deionized water to form a homogeneous and mixed solution under robust stirring. The pretreated nickel foam and the obtained solution were mixed into a 50-mL Teflon-lined stainless autoclave and kept at 120 °C for 5 h. After that, the Zn-Co precursor coated on Ni foam was washed with absolute ethanol and deionized water to remove the remaining reactants. After being dried at 60 °C for 12 h in a vacuum oven, the Zn-Co precursor active material was calcined at 400 °C for 2 h in air. The loading mass of the $ZnCo_2O_4$ active material can be obtained by measuring the weight change of the examples before and after hydrothermal and calcination process. The mass loading of $ZnCo_2O_4$ on Ni foam was 0.8 mg cm^{-2}.

Preparation of ZnCo$_2$O$_4$@NiWO$_4$ core-shell nanowire/nanosheet arrays

In a typical synthesis, $NiCl_2 \cdot 6H_2O$ (0.475 g) was dissolved into 30 mL distilled water by stirring for 10 min. Then, 30 mL distilled water containing $Na_2WO_4 \cdot 4H_2O$ (0.659 g) was

added dropwise and stirred for another 10 min. Then, the ZnCo$_2$O$_4$ on Ni foam was soaked into above solution in a Teflon-lined stainless steel autoclave, which was maintained at 140 °C for 4 h to fabricate ZnCo$_2$O$_4$@NiWO$_4$ core-shell nanostructure. Subsequently, the obtained ZnCo$_2$O$_4$@NiWO$_4$ precursor was respectively washed in distilled water and anhydrous ethanol and then dried at 60 °C overnight for next fabrication step. Finally, the precursor was annealed at 350 °C in air for 2 h to obtain ZnCo$_2$O$_4$@NiWO$_4$ core-shell nanowire/nanosheet arrays. The mass of core-shell hierarchical nanostructure loaded on nickel foam was measured to be 1.2 mg cm^{-2}.

Materials characterization

The crystal structure and chemical composition were evaluated by X-ray diffraction (XRD, Rigaku D/MAX D/MAX-3B) using Cu-Ka radiation (1.5418°A) at 40 kV, 100 mA. The morphological and nanostructured information of the samples were examined using field emission scanning electron microscopy (FESEM, SU 8010) and transmission electron microscope (TEM, JEOL/JEM 2100). The chemical elements and states were investigated using an X-ray photoelectron spectroscopy (XPS, PHI5600 XPS system).

Electrochemical measurements

Electrochemical performance of all samples was investigated in 2 M KOH aqueous solution using an electrochemical workstation (Zahner). The information of cyclic voltammetry (CV), galvanic charging/discharging (GCD), and electrochemical impedance spectroscopy (EIS) were obtained in a three-electrode system, where the as-prepared active materials (ZnCo$_2$O$_4$ and ZnCo$_2$O$_4$@NiWO$_4$ nanostructures) coated on nickel foam, Pt foil, and Hg/HgO were used as the working, counter, and reference electrodes, respectively. The CV property was respectively recorded from 0 to 0.8 V at different scan rates ranging from 5 to 50 mV s^{-1}. The GCD property was respectively studied in a potential between 0 and 0.5 V at the current densities ranging from 1 to 10 mA cm^{-2}. Electrochemical impedance spectra (EIS) were studied with a 5-mV AC voltage in a specific frequency range beginning from 0.01 Hz and ending to 100 kHz. The total area of the testing electrodes was approximately fixed to be ~ 1 × 1 cm^2.

Hybrid supercapacitor assembly and measurements

The asymmetric supercapacitor (ASC) was obtained by assembling ZnCo$_2$O$_4$@NiWO$_4$ nanowire/nanosheet arrays to be positive electrode and activated carbon (AC) as the negative electrode. Firstly, 80% of AC was mixed with 10% of acetylene black and 10% of polytetrafluoroethylene (PTFE) binder with the aid of NMP solvent. Then, the obtained mixture was loaded on the nickel foam at a pressure of 6 MPa and subsequently being dried in a vacuum oven at 60 °C overnight to form negative AC electrode. The loading mass of AC on nickel foam was controlled to be 4 mg as the negative electrode material. To prepare the polyvinyl alcohol-potassium hydroxide (PVA/KOH) electrolyte, 6 g PVA was dissolved into a 2 M KOH solution (60 mL) and heated at 85 °C under vigorous stirring until a homogeneous viscous solution appeared. The ZnCo$_2$O$_4$@NiWO$_4$ and AC electrodes were firstly immersed in 2 M KOH solution and maintained for 12 h. After, the assembled electrodes were taken out and immersed into the as-prepared PVA/KOH electrolyte with a cellulose separator for 10 min. Finally, an all-solid-state ASC was obtained by assembling the electrodes and cellulose separator into a sandwich structure, which was measured in a two-electrode system.

Results and discussion

Figure 1 shows the fabrication procedure of ZnCo$_2$O$_4$@NiWO$_4$ core-shell nanostructure. Initially, the ZnCo$_2$O$_4$ nanowire arrays, obtained from the first hydrothermal treatment followed by thermal treatment, were highly ordered aligned on Ni foam. Then, the NiWO$_4$ nanosheets were loaded on the surface of ZnCo$_2$O$_4$ nanowire arrays via the second hydrothermal method followed by annealing treatment. Figure 2 a presents top-view photograph of Ni foam before and after the loading of active materials. The color of Ni foam is changed from silver gray to pinkish purple due to the formation of Zn-Co precursor on the nickel foam. The surface of Ni foam turns from pinkish purple to black after thermal treatment. Fi`gure 2 b–g show the morphologies of the ZnCo$_2$O$_4$ nanowires and the ZnCo$_2$O$_4$@NiWO$_4$ core-shell nanostructure. Clearly, ZnCo$_2$O$_4$ nanowire arrays are uniformly and densely coated on nickel foam to guarantee the enough mass of active materials shown in Fig. 2b, c. Close observation of the ZnCo$_2$O$_4$ nanowire finds that the ZnCo$_2$O$_4$ nanowires are uniform in size, with average diameters of 100–200 nm and the length up to several microns (Fig. 2d). The well-separated growth of ZnCo$_2$O$_4$ nanowires on Ni foam can not only highly enhance mechanical adhesion between active materials and Ni foam but can also be accessible to the electrolyte, which reduces the contact resistance and leads to high capacitive performance. Correspondingly, yellow color can be seen on the current collector indicating the NiWO$_4$ covering on Ni foam as shown in Fig. 2a. Furthermore, the well-separated ZnCo$_2$O$_4$ nanowires with much open spaces can act as the backbone to guide the growth of NiWO$_4$ nanosheet shell. As shown in Fig. 2e–g, the surfaces of the ZnCo$_2$O$_4$ nanowire are covered by ultrathin and interconnected NiWO$_4$ nanosheets after the second hydrothermal treatment. The morphological and nanostructured features

Fig. 1 Fabrication procedure for the ZnCo$_2$O$_4$@NiWO$_4$ integrated electrode
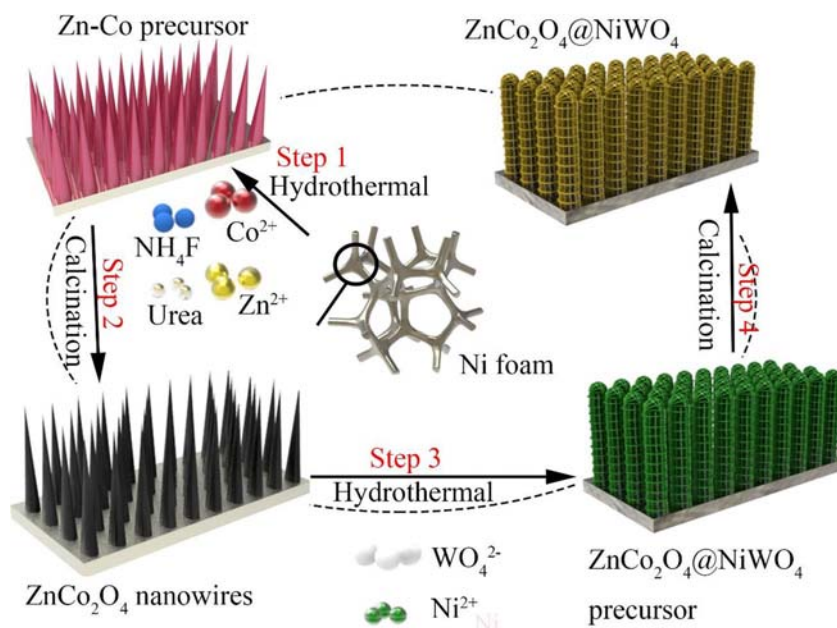
of ZnCo$_2$O$_4$@NiWO$_4$ core/shell were further characterized by TEM images as shown in Fig. 2h, i. The ZnCo$_2$O$_4$ nanowire substrates are typically coated with nanosized NiWO$_4$. The Zn, Co, O, Ni, and W elements can be clearly observed by EDS mapping as shown in Fig. 2j. Thus, the formation of the ZnCo$_2$O$_4$@NiWO$_4$ nanostructure was further confirmed. Moreover, the ultrathin NiWO$_4$ nanosheets are highly interconnected on ZnCo$_2$O$_4$ nanowires. The 3D core/shell hierarchical structure can guarantee abundant free space, which can offer more electroactive surface sites and further enhance the electrochemical capacitance. The crystal phases of as-prepared ZnCo$_2$O$_4$ nanowires and ZnCo$_2$O$_4$@NiWO$_4$ core-shell nanowire/nanosheet arrays were investigated by XRD shown in Fig. 3. The diffraction peaks of ZnCo$_2$O$_4$ nanowires at 18.9°, 31.2°, 36.8°, 38.5°, 44.7°, 55.6°, 59.3°, 65.1°, 74°, and 77.2° correspond well to the planes of (111), (220), (311), (222), (400), (331), (422), (511), (440), and (531), respectively, for the standard cubic spinel of ZnCo$_2$O$_4$ (JCPDS card no. 23-1390). The hybrid ZnCo$_2$O$_4$@NiWO$_4$ presents the diffraction peaks at 15.6°, 19.3°, 23.9°, 24.9°, 30.9°, 36.6°, 39.1°, 41.6°, 44.7°, 46.4°, 49°, 52.3°, 54.6°, 62.3°, 62.7°, 65.5°, 65.8°, 68.9°, 72.3°, and 72.6° and can be recognized as the planes of (010), (100), (011), (110), (−111), (020), (002), (200), (−102), (210), (−211), (−112), (−202), (212), (300), (032), (−113), (−141), (−302), and (−312) for NiWO$_4$ (JCPDS card no. 15-0755) [28]. Notably, the weak diffraction peaks indicate that as-prepared ZnCo$_2$O$_4$@NiWO$_4$ electrode consists of very small crystallines, which are usually linked with high electrochemical performance [33, 34]. The surface composition and chemical states of as-prepared ZnCo$_2$O$_4$@NiWO$_4$ electrode was investigated by XPS shown in Fig. 4. In Fig. 4a, the C 1s peak is related to underlying carbon tape for mounting samples, while the characteristic peaks of Zn, Co, O, Ni, and W elements are consistent with the core/shell structure of ZnCo$_2$O$_4$@NiWO$_4$. Figure 4 b exhibits a major peak at the binding energy of 1024.5 eV, which can be associated with the Zn 2$p_{3/2}$ [19]. Figure 4 c exhibits two major peaks located at the binding energy of 780.4 and 795.2 eV, respectively. The two peaks are related to the Co 2$p_{3/2}$ and Co 2$p_{1/2}$ energy level, respectively, indicating the characteristics oxidation states Co^{2+} and Co^{3+} [13]. As shown in Fig. 4d, the two main peaks at 529.2 and 530.8 eV are respectively attributed to the characteristic bands of the oxygen atoms in the oxides of ZnCo$_2$O$_4$ and NiWO$_4$, as well as the oxygen from hydroxide ions. The minor peak at 532.2 eV is corresponding to surface-bound water or adsorbed oxygen [35]. Figure 4 e reveals two major peaks at 856.7 and 872.6 eV, which are respectively associated with Ni 2$p_{3/2}$ and Ni 2$p_{1/2}$ levels, as well as two shake-up satellites [5]. Figure 4 f shows two peaks at 34.1 eV and 36.3 eV, which correspond to W 4$f_{7/2}$ and W 4$f_{5/2}$, respectively, revealing an oxidation state of W^{6+} [7]. The ZnCo$_2$O$_4$ nanowire arrays and ZnCo$_2$O$_4$@NiWO$_4$ nanowire/nanosheet arrays in situ grown on nickel foams could be directly evaluated by their electrochemical property without extra binder. Figure 5 a shows the CV properties of ZnCo$_2$O$_4$ and ZnCo$_2$O$_4$@NiWO$_4$ electrodes at a sweep rate of 20 mV s^{-1}. As expected, the area integrated within CV curve of the core-shell electrode is larger than that of the single electrode, illustrating that the core-shell electrode can reach a larger storage capacity. It can be understood that the additional NiWO$_4$ shells can absorb more cations on the electrode surface for charge storage [36]. In addition, GCD curves were measured at 1 mA cm^{-2} to estimate the specific capacitance of the two electrodes, as shown in Fig. 5b. The ZnCo$_2$O$_4$@NiWO$_4$ core/shell nanosheet array electrode spends 1069.0 s completing one discharge process, which is

Fig. 2 Corresponding top-view photograph of **a** the ZnCo$_2$O$_4$@NiWO$_4$ core-shell nanostructure at each step (samples 1, 2, 3, 4, and 5 refer to the pure Ni foam, Zn-Co precursor, ZnCo$_2$O$_4$ nanowires, ZnCo$_2$O$_4$@NiWO$_4$ precursor, ZnCo$_2$O$_4$@NiWO$_4$, respectively). SEM images of **b**–**d** ZnCo$_2$O$_4$ and **e**–**g** ZnCo$_2$O$_4$@NiWO$_4$ samples. **h**, **i** TEM images of ZnCo$_2$O$_4$@NiWO$_4$ nanosheet arrays with different magnifications. **j** EDS mapping of the ZnCo$_2$O$_4$@NiWO$_4$ electrode
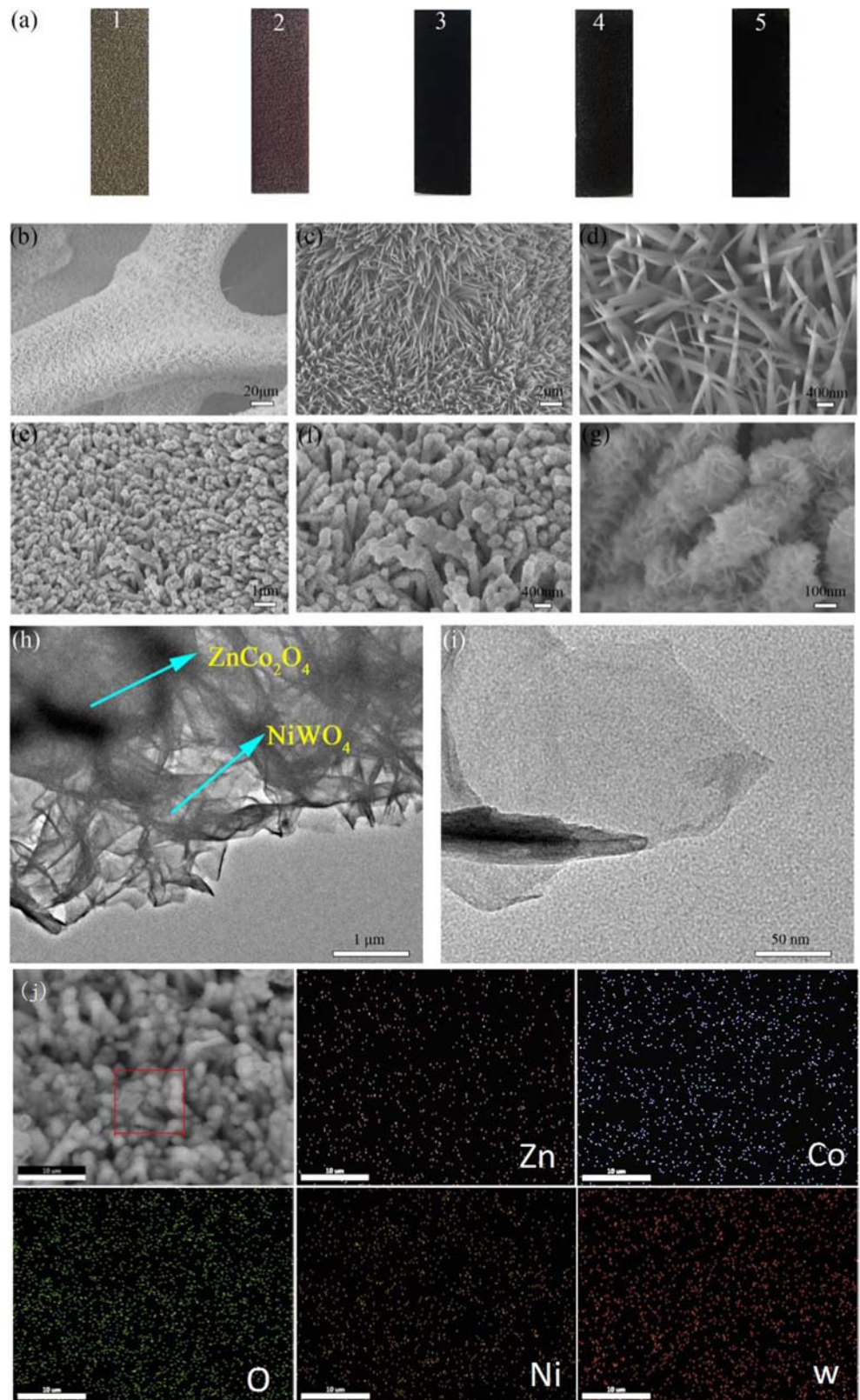
about 2 times that of the ZnCo$_2$O$_4$ electrode (521.0 s). Since the ZnCo$_2$O$_4$@NiWO$_4$ electrode shows much higher specific capacitance, the electrochemical properties of ZnCo$_2$O$_4$@NiWO$_4$ electrode were systematically measured as a function of scan rate (current density). Figure 5 c shows the CV curves of the ZnCo$_2$O$_4$@NiWO$_4$ electrode obtained at
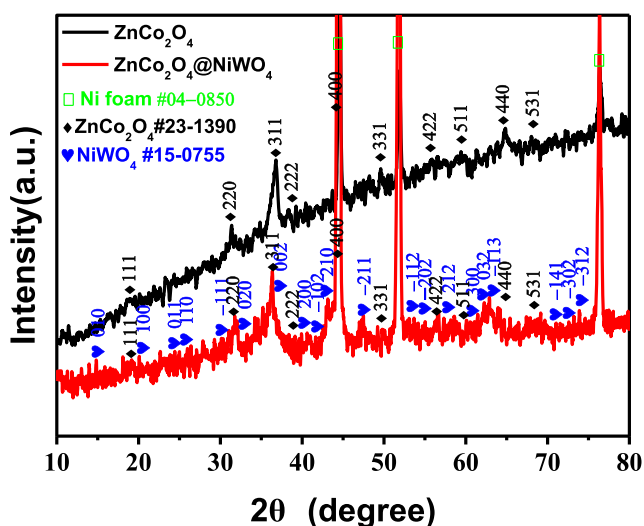
Fig. 3 Typical XRD patterns of the $ZnCo_2O_4$ and $ZnCo_2O_4@NiWO_4$ samples, which corresponds well to the standard diffraction patterns of Zinc cobalt oxide (JCPDS card no. 23-1390) and nickel tungsten oxide (JCPDS card No. 15-0755)

different scan rates in a potential window from 0 to 0.7 V. A pair of redox peaks clearly appeared in the CV curves of $ZnCo_2O_4@NiWO_4$ core-shell electrode, in which one peak appeared at 0.3 V (negative scan) while the other peak appeared at 0.55 V (positive scan), featured by faradaic redox mechanism. The slight shift of redox peaks at various sweep rates is resulted from the polarization phenomenon [37]. Figure 5 d presents GCD curves of the $ZnCo_2O_4@NiWO_4$ in a potential window ranging from 0 to 0.5 V, scanned as a function of current densities. The corresponding discharge time is found to be 1069, 506, 164, 76, and 49 s, respectively, measured at 1, 2, 5, 7.5, and 10 mA cm^{-2}. The area-specific capacitance C_a (F cm^{-2}) and mass-specific capacitance C_m (F g^{-1}) can be respectively calculated by the following equation [1, 38]:

$$C_a = \frac{i \Delta t}{s \Delta v} \text{ and } C_m = \frac{i \Delta t}{m \Delta v} \quad (1)$$

where i signifies the discharge current, S is the area of nickel foam immersed in electrolyte, and m is the loading mass of active material on nickel foam, ΔV is the potential window, and Δt designate the discharging time, respectively. For comparison purpose, the areal capacitances of both $ZnCo_2O_4$ and $ZnCo_2O_4@NiWO_4$ electrodes are calculated and plotted as the current density increases, as showed in Fig. 5e. The areal capacitance of $ZnCo_2O_4$ electrode are calculated to be 1.040, 0.864, 0.607, 0.427, and 0.340 F cm^{-2} at the current densities of 1, 2, 5, 7.5, and 10 mA cm^{-2}, respectively. Correspondingly, the specific capacitance of $ZnCo_2O_4$ electrode are found to be 1300 F g^{-1} at a current density 1 A g^{-1}, which is higher than that of many reported $ZnCo_2O_4$ electrode ranged from 689 to 1664 F g^{-1} [6, 39–41]. The areal capacitances of the $ZnCo_2O_4@NiWO_4$

electrode are found to be 2.140, 2.024, 1.600, 1.080, and 0.760 F cm^{-2} at the current densities of 1, 2, 5, 7.5, and 10 mA cm^{-2}, respectively. Clearly, the $ZnCo_2O_4@NiWO_4$ electrode exhibit much higher areal capacitances than that of single $ZnCo_2O_4$ electrode at all current densities. The corresponding volumetric capacitances are 21.40, 20.24, 16.00, 10.80, and 7.60 F cm^{-3}, and specific capacitances are found to be 1782, 1687, 1373, 950, and 817 F g^{-1}, respectively. Therefore, the as-prepared core-shell electrode show higher specific capacitance than that of similar core-shell nanostructure such as $ZnCo_2O_4@NiCo_2O_4$ (1476 F g^{-1} at 1 A g^{-1}) [42], $ZnCo_2O_4@Ni_3V_2O_8$ (1734 F g^{-1} at 1 A g^{-1}) [43], $NiCo_2O_4@NiWO_4$ (1384 F g^{-1} at 1 A g^{-1}) [28], and $NiMoO_4@NiWO_4$ (1290 F g^{-1} at 1 A g^{-1}) [7]. The enhanced performance can be attributed to the 3D hierarchical core/shell structure and the synergic effects of two different binary transition metal oxides. A higher current density leads to a lower area capacitance. The reason is that the diffusion of the ions is quite slow and only the surface of the electrode could be utilized to provide active sites for charge storage. Cycling performance is also a significant parameter to study the quality of electrode for practical applications. Figure 5 f shows the capacitance retention during 5000 GCD cycles at 5 mA cm^{-2}. At the initial measurement, there is a gradual activation process of the active material, which could contribute to the slight increase of capacitance. The similar phenomenon can be found in many previous literatures [44–46]. Furthermore, it is found that the $ZnCo_2O_4@NiWO_4$ electrode presents an outstanding robust cycling stability with as high as 95.3% capacitance retained after 5000 successive GCD cycles, which is much higher than 90.9% capacitance retention of the single $ZnCo_2O_4$ electrode. The enhanced cycling stability of $ZnCo_2O_4@NiWO_4$ electrode is possibly attributed to the increased electrical conductivity of core-shell-nanostructured electrode, which could be confirmed by the EIS analysis. Figure 5 g shows the comparison of Nyquist plots between the single $ZnCo_2O_4$ and $ZnCo_2O_4@NiWO_4$ electrodes, which was recorded in a frequency range from 0.01 to 100 kHz. The two electrodes exhibit similar impedance spectra with a quasi-semicircle in the high frequency region and a slope in the low frequency region. The EIS curves can be modeled by the equivalent circuit shown in Fig. 5h. As expected, the internal resistance (R_s) of the $ZnCo_2O_4@NiWO_4$ electrode (1.053 Ω) is slightly lower than that of $ZnCo_2O_4$ electrode (1.063 Ω), indicating the enhanced electrical conductivity of $ZnCo_2O_4@NiWO_4$ electrode [47]. Furthermore, the $ZnCo_2O_4@NiWO_4$ electrode exhibits a rather smaller semicircle than that of $ZnCo_2O_4$ electrode, demonstrating that the $ZnCo_2O_4@NiWO_4$ electrode has a much lower charge-transfer resistance (R_{ct}) 1.526 Ω than 2.633 Ω of the $ZnCo_2O_4$ electrode at electrode−electrolyte interface. In the low frequency region, $ZnCo_2O_4@NiWO_4$ electrode exhibits a more vertical line, revealing the lower diffusion resistance within the electrode [48]. The above results demonstrate the enhanced properties of the $ZnCo_2O_4@NiWO_4$ electrode comes from the

Fig. 4 XPS spectra of the ZnCo$_2$O$_4$@NiWO$_4$ electrode. **a** Survey spectrum. **b** Zn 2*p*. **c** Co 2*p*. **d** O 1*s*. **e** Ni 2*p*. **f** W 4*f*
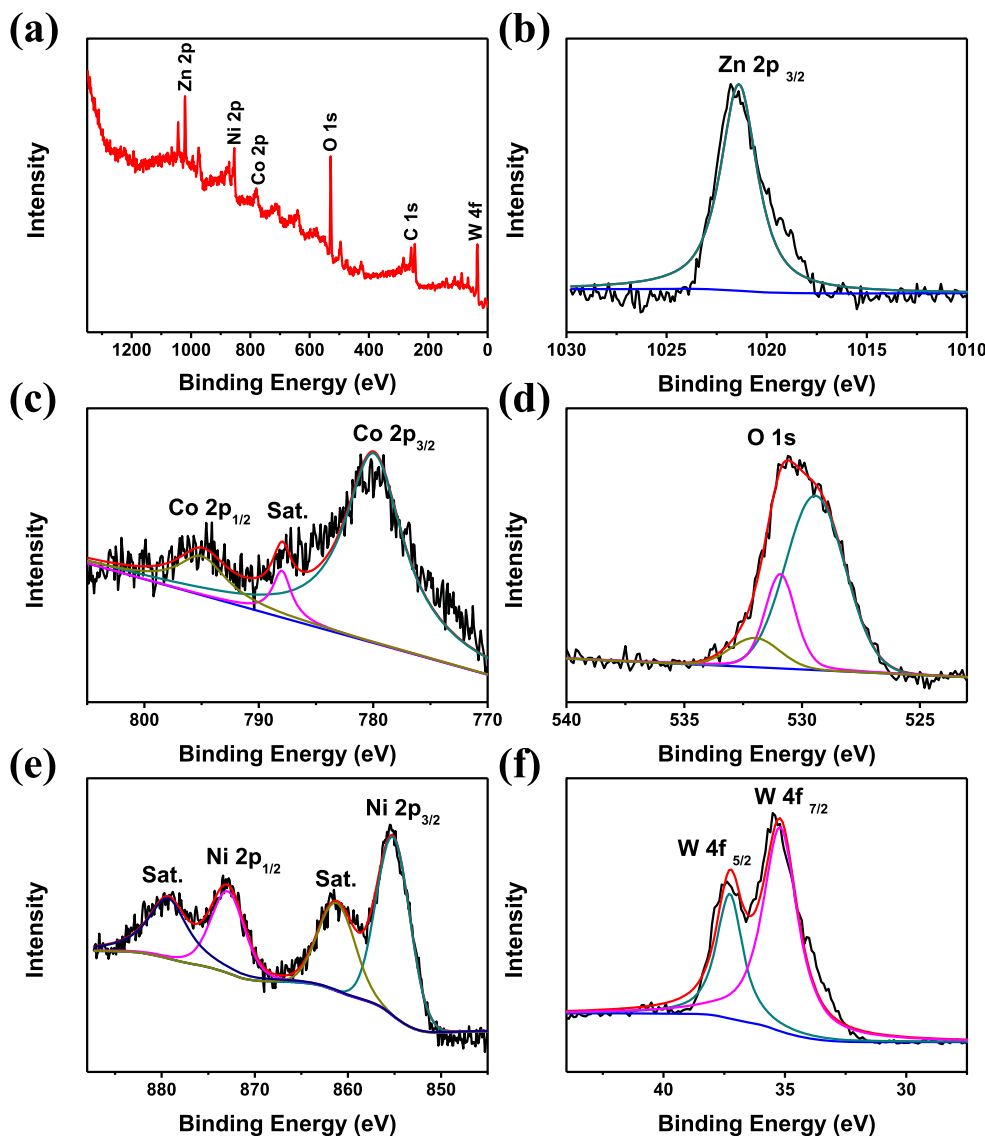
synergistic effects from the two components, the fast charge diffusion and quite low electro-transfer resistance [8]. To demonstrate the more reliable energy storage capability, all-solid-state ASC device of as-obtained ZnCo$_2$O$_4$@NiWO$_4$//AC has been and assembled and investigated by integrating the positive electrode of ZnCo$_2$O$_4$@NiWO$_4$ core/shell arrays, the negative electrode of AC with PVA-KOH gel electrolyte, as illustrated in Fig. 6a. Figure 6 b presents the CV characteristics of the ASC device measured at the scan rates from 10 to 100 mV s^{-1}. Clearly, the shape of CV curves and redox peaks are maintained at high scan rate such as 100 mV s^{-1}, indicating the fast ion transport and excellent reversible faradaic reaction. Figure 6 c presents the GCD properties of the ASC device obtained at various current densities of 5, 10, 15, and 20 mA cm^{-2}. The nearly symmetric GCD curves also demonstrate the ZnCo$_2$O$_4$@NiWO$_4$//AC ASC owns a strongly reversible reaction process. Correspondingly, the discharge time is estimated to be 212, 99, 58, and 43 s,
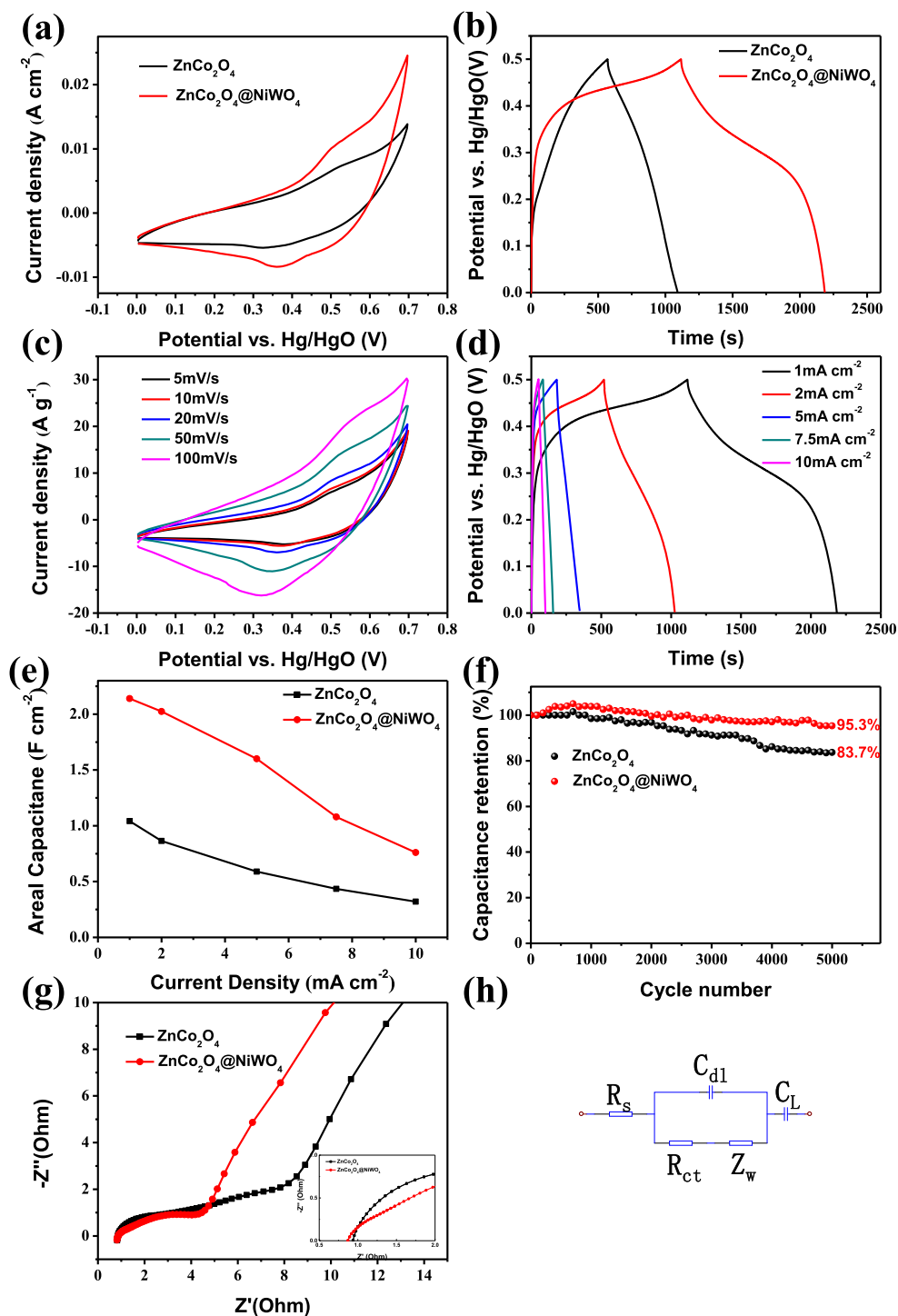
respectively. The specific capacitance of ASC device at different current densities could be calculated by Eq. (2), where *m* is the total mass of all active materials excluding the current collector. The mass ratio of ZnCo$_2$O$_4$@NiWO$_4$ arrays and AC can be obtained based on the balance rule of positive and negative charges ($q^+ = q^-$) presented in the following equation [49]:

$$q = C\Delta Vm \tag{2}$$

$$\frac{m_+}{m_-} = \frac{C_-\Delta V_-}{C_+\Delta V_+} \tag{3}$$

where *C* is the capacitance of the each electrode (F g^{-1}), ΔV is the potential window (*V*), and *m* represent the mass of each electrode (*g*). The specific capacitance is calculated to be 135, 126, 112, and 110 F g^{-1}, respectively, corresponds to different

Fig. 5 **a** Comparison of CV and **b** GCD curves between the $ZnCo_2O_4$ and $ZnCo_2O_4@NiWO_4$ electrodes. **c** CV and **d** GCD curves of the $ZnCo_2O_4@NiWO_4$ electrode. **e** Areal capacitance vs. current density for the $ZnCo_2O_4$ and $ZnCo_2O_4@NiWO_4$ electrodes. **f** Comparison of cycling behavior of the $ZnCo_2O_4$ and $ZnCo_2O_4@NiWO_4$ electrodes. **g** EIS and the related enlarged Nyquist plots in the high frequency region. **h** Corresponding electrical equivalent circuit of the $ZnCo_2O_4$ and $ZnCo_2O_4@NiWO_4$ electrodes

applied currents of 5, 10, 15, and 20 mA cm^{-2}. Additionally, the energy density (E) and power density (P) are calculated by the following equation [1]:

$$E = \frac{1}{7.2} C (\Delta V)^2 \quad (4)$$

$$P = \frac{3600 \times E}{t} \quad (5)$$

where C is the specific capacitance (F g^{-1}), ΔV is the potential window (V), t is the discharging time (s). From the ragone plot shown in Fig. 6e, the energy densities of the ASC device are found to be 42.2, 39.4, 35.0, and 34.3 Wh kg^{-1} at power densities of 716, 1432, 2172, and 3087 W kg^{-1}, respectively. The result is much higher than that of single $ZnCo_2O_4$//AC (34 Wh/kg at 1800 W/kg) [50] and $NiWO_4$//AC (25.3 Wh/kg at 684 W/kg) [29], respectively. Furthermore, the as-prepared

Fig. 6 **a** Schematic illustration of the ACS device. **b** CV and **c** GCD curves of ACS device. **d** The mass- and area-specific capacitances changed as a function of current density. **e** Ragone plot. **f** EIS and the related enlarged Nyquist plots in the high frequency region of ACS device
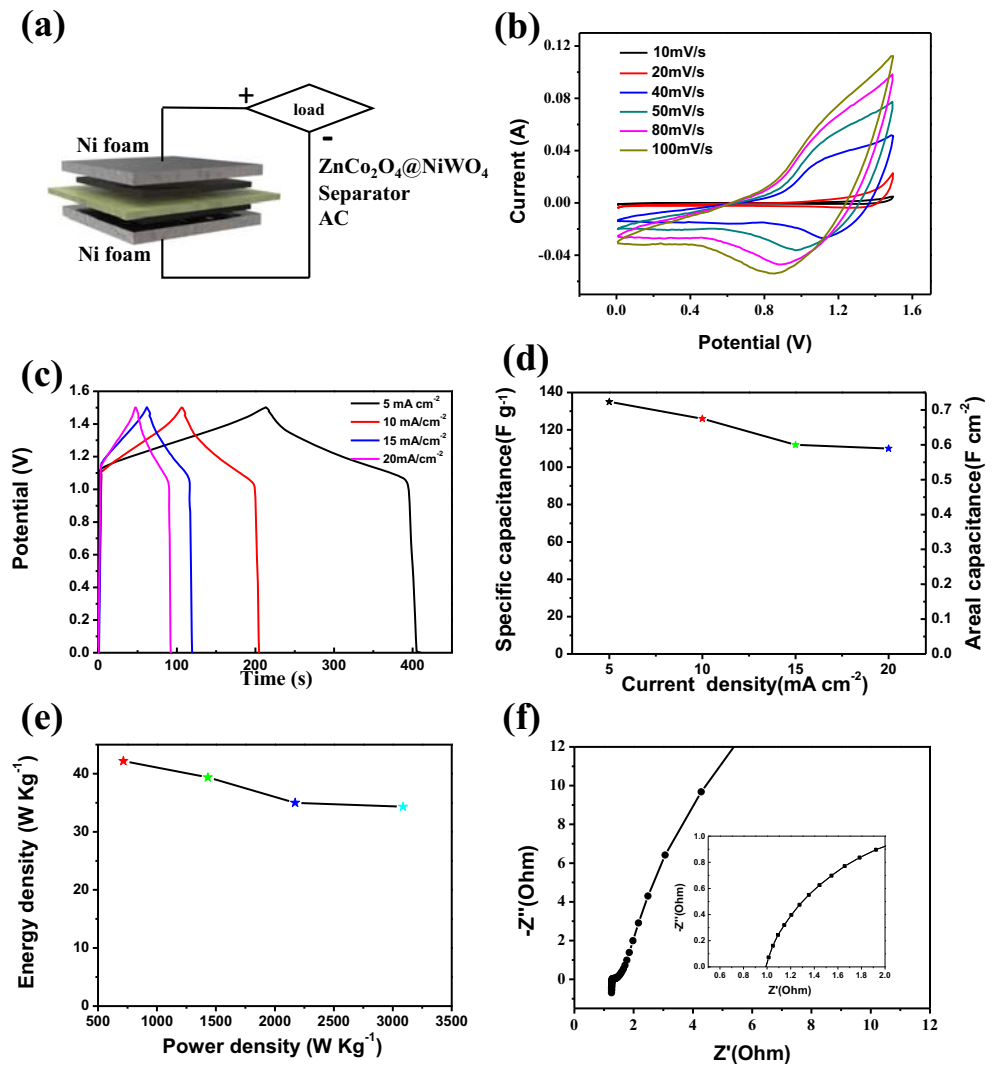
electrode also shows much higher energy density and power density than that of similar core-shell nanostructure such as $ZnCo_2O_4@Ni_xCo_{2x}(OH)_{6x}$//AC (26.2 Wh/kg at 511.8 W/kg) [24] and $ZnCo_2O_4@MO_2/\alpha\text{-}Fe_2O_3$ (37.8 Wh/kg at 684 W/kg) [51]. From the EIS spectrum and the inset of enlarged Nyquist plots in the high frequency region shown in Fig. 6f, the ASC device also presents the series resistance of 1.053 Ω and the charge transfer resistance of 1.526 Ω, further confirming the higher conductivity and more efficient charge transport within the electrode.

Conclusions

In conclusion, 3D, string-like, core-shell, heterostructured $ZnCo_2O_4@NiWO_4$ nanowire/nanosheet arrays are grown on 3D nickel foam substrate by reliable, two-step hydrothermal processes and subsequent annealing treatment. The $ZnCo_2O_4@NiWO_4$ hybrid electrode delivers a specific capacitance as high as 1782 F g^{-1} at 1 mA cm^{-2} (2.14 F cm^{-2}) and

especially high cycling stability (95.3% capacitance retention after 5000 cycles), which are much higher than individual $ZnCo_2O_4$ electrode without the $NiWO_4$ shell. Such fascinating electrochemical performance benefits from the 3D string-like core-shell nanostructure and synergistic effects of the contributions from both $ZnCo_2O_4$ nanowire core and $NiWO_4$ shell nanosheets, which could provide more active sites for charge storage, facilitate quick charge penetration of electrolyte, and increase diffusion of ions. Therefore, constructing string-like core-shell hybrid nanowire/nanosheet arrays with two different binary transition metal oxides may serve to be a potential way to develop high-performance supercapacitors

References

1. Zhao J, Li Y, Wang G, Wei T, Liu Z, Cheng K, Ye K, Zhu K, Cao D, Fan Z (2017) Enabling high-volumetric-energy-density supercapacitors: designing open, low-tortuosity heteroatom-doped porous carbon-tube bundle electrodes. J Mater Chem A 44:23085–23093

2. Singh SB, Singh TI, Kim NH, Lee JH (2019) A core–shell MnO_2@Au nanofiber network as a high-performance flexible transparent supercapacitor electrode. J Mater Chem A 17:10672–10683

3. Wu D, Zhong W (2019) A new strategy for anchoring a functionalized graphene hydrogel in a carbon cloth network to support a lignosulfonate/polyaniline hydrogel as an integrated electrode for flexible high areal-capacitance supercapacitors. J Mater Chem A 10:5819–5830

4. Wu C, Cai J, Zhu Y, Zhang K (2017) Hybrid reduced graphene oxide nanosheet supported Mn-Ni-Co ternary oxides for aqueous asymmetric supercapacitors. ACS Appl Mater Interfaces 22:19114–19123

5. Cheng J, Lu Y, Qiu K, Yan H, Xu J, Han L, Liu X, Luo J, Kim JK, Luo Y (2015) Hierarchical core/shell $NiCo_2O_4$@$NiCo_2O_4$ nanocactus arrays with dual-functionalities for high performance supercapacitors and Li-ion batteries. Sci Rep, 12099

6. Liu B, Liu B, Wang Q, Wang X, Xiang Q, Chen D, Shen G (2013) New energy storage option: toward $ZnCo_2O_4$ nanorods/nickel foam architectures for high-performance supercapacitors. ACS Appl Mater Interfaces 20:10011–10017

7. Reddy AE, Anitha T, Muralee Gopi CVV, Srinivasa Rao S, Kim HJ (2018) $NiMoO_4$@$NiWO_4$ honeycombs as a high performance electrode material for supercapacitor applications. Dalton Trans 27:9057–9063

8. Wang, J.; Zhang, L.; Liu, X.; Zhang, X.; Tian, Y.; Liu, X.; Zhao, J.; Li, Y. (2017) Assembly of flexible $CoMoO_4$@$NiMoO_4$·xH_2O and Fe_2O_3 electrodes for solid-state asymmetric supercapacitors. Sci Rep, 41088

9. Gu Z, Zhang X (2016) $NiCo_2O_4$@$MnMoO_4$ core–shell flowers for high performance supercapacitors. J Mater Chem A 21:8249–8254

10. Wang R, Wu S, Lv Y, Lin Z (2014) Partially crystalline Zn_2GeO_4 nanorod/graphene composites as anode materials for high performance lithium ion batteries. Langmuir 27:8215–8220

11. Xu J, Sun Y, Lu M, Wang L, Zhang J, Tao E, Qian J, Liu X (2018) Fabrication of the porous MnCo2O4 nanorod arrays on Ni foam as an advanced electrode for asymmetric supercapacitors. Acta Mater 162-174

12. Wang S, Pu J, Tong Y, Cheng Y, Gao Y, Wang Z (2014) $ZnCo_2O_4$ nanowire arrays grown on nickel foam for high-performance pseudocapacitors. J Mater Chem A 15:5434–5440

13. Bao F, Wang X, Zhao X, Wang Y, Ji Y, Zhang H, Liu X (2014) Controlled growth of mesoporous $ZnCo_2O_4$ nanosheet arrays on Ni foam as high-rate electrodes for supercapacitors. RSC Adv 5:2393–2397

14. Wu H, Lou Z, Yang H, Shen G (2015) A flexible spiral-type supercapacitor based on $ZnCo_2O_4$ nanorod electrodes. Nanoscale 5:1921–1926

15. Zhong S, Zhang H, Fu J, Shi H, Wang L, Zeng W, Liu Q, Zhang G, Duan H (2018) In-situ synthesis of 3D carbon coated zinc-cobalt bimetallic oxide networks as anode in lithium-ion batteries. ChemElectroChem 13:1708–1716

16. Wang Q, Zhu L, Sun L, Liu Y, Jiao L (2015) Facile synthesis of hierarchical porous $ZnCo_2O_4$ microspheres for high-performance supercapacitors. J Mater Chem A 3:982–985

17. Zhao J, Li C, Zhang Q, Zhang J, Wang X, Lin Z, Wang J, Lv W, Lu C, Wong C-p, Yao Y (2017) An all-solid-state, lightweight, and flexible asymmetric supercapacitor based on cabbage-like $ZnCo_2O_4$ and porous VN nanowires electrode materials. J Mater Chem A 15:6928–6936

18. Venkatachalam V, Alsalme A, Alswieleh A, Jayavel R (2017) Double hydroxide mediated synthesis of nanostructured $ZnCo_2O_4$ as high performance electrode material for supercapacitor applications. Chem Eng J 474-483

19. Liu T, Wang W, Yi M, Chen Q, Xu C, Cai D, Zhan H (2018) Metal-organic framework derived porous ternary $ZnCo_2O_4$ nanoplate arrays grown on carbon cloth as binder-free electrodes for lithium-ion batteries. Chem Eng J 454-462

20. Mary AJC; Bose AC (2017) Facile synthesis of $ZnCo_2O_4$/rGO nanocomposite for effective supercapacitor application. 050093

21. Sahoo S, Shim J-J (2016) Facile synthesis of three-dimensional ternary $ZnCo_2O_4$/reduced graphene oxide/NiO composite film on nickel foam for next generation supercapacitor electrodes. ACS Sustain Chem Eng 1:241–251

22. Ru Q, Song X, Mo Y, Guo L, Hu S (2016) Carbon nanotubes modified for $ZnCo_2O_4$ with a novel porous polyhedral structure as anodes for lithium ion batteries with improved performances. J Alloys Compd 586-592

23. Sun Z, Ai W, Liu J, Qi X, Wang Y, Zhu J, Zhang H, Yu T (2014) Facile fabrication of hierarchical ZnCo2O4/NiO core/shell nanowire arrays with improved lithium-ion battery performance. Nanoscale 12:6563–6568

24. Fu W, Wang Y, Han W, Zhang Z, Zha H, Xie E (2016) Construction of hierarchical ZnCo2O4@NixCo2x(OH)6x core/shell nanowire arrays for high-performance supercapacitors. J Mater Chem A 1:173–182

25. Chen S, Zhang Z, Zeng W, Chen J, Deng L (2019) Construction of $NiCo_2S_4$@$NiMoO_4$ core-shell nanosheet arrays with superior electrochemical performance for asymmetric supercapacitors. ChemElectroChem 2:590–597

26. Chen S; Chandrasekaran S; Cui S; Li Z; Deng G; Deng L (2019) Self-supported $NiMoO_4$@$CoMoO_4$ core/sheath nanowires on conductive substrates for all-solid-state asymmetric supercapacitors. J Electroanal Chem, 113153

27. Xu J, Sun Y, Lu M, Wang L, Zhang J, Qian J, Liu X (2018) Fabrication of hierarchical $MnMoO_4$·H_2O@MnO_2 core-shell nanosheet arrays on nickel foam as an advanced electrode for asymmetric supercapacitors. Chem Eng J 1466-1476

28. Chen S, Yang G, Jia Y, Zheng H (2017) Three-dimensional $NiCo_2O_4$@$NiWO_4$ core–shell nanowire arrays for high-performance supercapacitors. J Mater Chem A 3:1028–1034

29. Niu L, Li Z, Xu Y, Sun J, Hong W, Liu X, Wang J, Yang S (2013) Simple synthesis of amorphous $NiWO_4$ nanostructure and its application as a novel cathode material for asymmetric supercapacitors. ACS Appl Mater Interfaces 16:8044–8052

30. Mani, S.; Vediyappan, V.; Chen, S. M.; Madhu, R.; Pitchaimani, V.; Chang, J. Y.; Liu, S. B. (2016) Hydrothermal synthesis of $NiWO_4$ crystals for high performance non-enzymatic glucose biosensors. Sci Rep, 24128

31. Li M, Yokoyama S, Takahashi H, Tohji K (2019) Bandgap engineering of $NiWO_4$/CdS solid Z-scheme system via an ion-exchange reaction. Appl Catal B Environ 284-291

32. Anis SF, Lalia BS, Mostafa AO, Hashaikeh R (2017) Electrospun nickel–tungsten oxide composite fibers as active electrocatalysts for hydrogen evolution reaction. J Mater Sci 12:7269–7281

33. Lu Q, Chen JG, Xiao JQ (2013) Nanostructured electrodes for high-performance pseudocapacitors. Angew Chem Int Ed Eng 7:1882–1889

34. Zhang Z, Zhang X, Feng Y, Wang X, Sun Q, Yu D, Tong W, Zhao X, Liu X (2018) Fabrication of porous $ZnCo_2O_4$ nanoribbon arrays on nickel foam for high-performance supercapacitors and lithium-ion batteries. Electrochim Acta 823-829

35. Pan Y, Zeng W, Li L, Zhang Y, Dong Y, Cao D, Wang G, Lucht BL, Ye K, Cheng K (2017) A facile synthesis of $ZnCo_2O_4$ nanocluster particles and the performance as anode materials for lithium ion batteries. Nano Lett 2:20

36. Yu L, Zhang G, Yuan C, Lou XW (2013) Hierarchical $NiCo_2O_4$@MnO_2 core-shell heterostructured nanowire arrays on Ni foam as high-performance supercapacitor electrodes. Chem Commun (Camb) 2:137–139

37. Gujar TP, Shinde VR, Lokhande CD, Kim W-Y, Jung K-D, Joo O-S (2007) Spray deposited amorphous RuO_2 for an effective use in electrochemical supercapacitor. Electrochem Commun 3:504–510

38. Samdani KJ, Park JH, Joh DW, Lee KT (2018) Self-assembled Bi_2MoO_6 nanopetal array on carbon spheres toward enhanced supercapacitor performance. ACS Sustain Chem Eng

39. Wang S, Teng Y, Liu X, Yu D, Meng YN, Wu Y, Sun S, Zhao X, Liu X (2019) Facile synthesis of mesoporous ZnCo2O4 nanowire arrays and nanosheet arrays directly grown on nickel foam for high-performance supercapacitors. Inorg Chem Commun 16-22

40. Xu L, Zhao Y, Lian J, Xu Y, Bao J, Qiu J, Xu L, Xu H, Hua M, Li H (2017) Morphology controlled preparation of ZnCo 2 O 4 nanostructures for asymmetric supercapacitor with ultrahigh energy density. Energy 296-304

41. Zhou, Y.; Chen, L.; Jiao, Y.; Li, Z.; Gao, Y. (2019) Controllable fabrication of ZnCo2O4 ultra-thin curved sheets on Ni foam for high-performance asymmetric supercapacitors. Electrochim Acta, 388–394

42. Huang Y, Miao YE, Lu H, Liu T (2015) Hierarchical ZnCo2O4 @NiCo2O4 core-sheath nanowires: bifunctionality towards high-performance supercapacitors and the oxygen-reduction reaction. Chemistry 28:10100–10108

43. Huang Y, Feng X, Li C, Li Y, Chen X, Gao X, Chen C, Guang Z, Liu P (2019) Construction of hydrangea-like ZnCo2O4@Ni3V2O8 hierarchical nanostructures for asymmetric all-solid-state supercapacitors. Ceram Int 12:15451–15457

44. Peng L, Lv L, Wan H, Ruan Y, Ji X, Liu J, Miao L, Wang C, Jiang J (2017) Understanding the electrochemical activation behavior of Co(OH)2 nanotubes during the ion-exchange process. Materials Today Energy 122-131

45. Lv L, Xu K, Wang C, Wan H, Ruan Y, Liu J, Zou R, Miao L, Ostrikov, K, Lan Y, Jiang J (2016) Intercalation of glucose in NiMn-layered double hydroxide nanosheets: an effective path way towards battery-type electrodes with enhanced performance. Electrochim Acta 35-43

46. Chen H, Jiang J, Zhang L, Qi T, Xia D, Wan H (2014) Facilely synthesized porous NiCo2O4 flowerlike nanostructure for high-rate supercapacitors. J Power Sources 28-36

47. Lv L, Zha D, Ruan Y, Li Z, Ao X, Zheng J, Jiang J, Chen HM, Chiang WH, Chen J, Wang C (2018) A universal method to engineer metal oxide-metal-carbon interface for highly efficient oxygen reduction. ACS Nano 3:3042–3051

48. Lv L, Li Z, Xue K-H, Ruana Y, Ao X, Wan H, Miao X, Zhang B, Jiang J, Wang C, Ostrikov KK (2018) Tailoring the electrocatalytic activity of bimetallic nickel-iron diselenide hollow nanochains for water oxidation. Nano Energy 275-284

49. Ruan Y, Lv L, Li Z, Wang C, Jiang J (2017) Ni nanoparticles@Ni-Mo nitride nanorod arrays: a novel 3D-network hierarchical structure for high areal capacitance hybrid supercapacitors. Nanoscale 45:18032–18041

50. Dianmei Songa JZ, Lia J, Pua T, Huanga B, Zhaoa C, Xiea L, Lingyun Chena B* (2017) Free-standing two-dimensional mesoporous ZnCo2O4 thin sheets consisting of 3D ultrathin nanoflake array frameworks for high performance asymmetric supercapacitor. Electrochim Acta 257:455–464

51. Ma W, Nan H, Gu Z, Geng B, Zhang X (2015) Superior performance asymmetric supercapacitors based on ZnCo2O4@MnO2 core–shell electrode. J Mater Chem A 10:5442–5448